PERGAMON

International Journal of Heat and Mass Transfer 41 (1998) 4351–4373

International Journal of HEAT and MASS TRANSFER

# Dynamic simulation of the vertical zone-melting crystal growth

C. W. Lan*, D. T. Yang

*Chemical Engineering Department, National Central University, Chung-Li, Taiwan 32054, Republic of China*

Received 10 April 1997; in final form 28 July 1997

**Abstract**

Dynamic behavior of heat transfer, fluid flow, and interfaces in the vertical zone-melting (VZM) crystal growth is studied numerically. The model, which is governed by axisymmetric unsteady-state momentum and heat transfer and interface balance in the system, is solved by a robust finite-volume method. Single crystal growth of $NaNO_3$ in a computer-controlled transparent multizone furnace is simulated as examples. The effects of gravity levels and heater temperature are considered. Multiple steady states obtained at stationary cases are used as initial conditions to illustrate the transient response and the stability of the VZM crystal growth to the pulse and step changes in thermal environments. For unstable cases, periodically oscillatory flow and growth rate occurring at intermediate values of the Rayleigh number are observed. The upper flow cells beneath the feed front seems to be responsible to the instability, and this is consistent with the observation during crystal growth experiments. For stable cases, a steady state can be achieved smoothly, and the calculated results are in good agreement with the ones from a pseudo steady-state model. 

**Nomenclature**

$a$ width parameter in $T_a$
$C_p$ specific heat
$\mathbf{e}_z$ unit vector in $z$-direction
$\mathbf{f}$ residual vector
$g$ gravitational acceleration
$h$ heat transfer coefficient
$h_c$ height of growth front
$h_f$ height of feed front
$I$ flux through the CV faces
$k$ thermal conductivity
$L$ length of ampoule
$\mathbf{n}$ unit normal vector
$Pr$ Prandtl number, $\nu/\alpha$
$r$ cylindrical coordinate
$Ra$ Rayleigh number, $\beta_T R_c^3 g(T_{max}-T_m)/\nu\alpha$
$R_a$ radius of ampoule
$R_c$ radius of crystal
$t$ time
$T$ temperature
$T_a$ ambient temperature distribution
$T_{a\infty}$ background ambient temperature
$T_m$ melting point
$T_p$ peak heater temperature
$u$ $r$-component of velocity
$U_{heater}$ heater moving speed
$U_0$ ampoule pulling speed
$v$ $z$-component of velocity
$V$ volume
$x$ solution vector
$z$ cylindrical coordinate.

*Greek symbols*

$\alpha$ thermal diffusivity
$\beta_T$ thermal expansion coefficient
$\varepsilon$ emissivity
$\eta$ curvilinear coordinate
$\nu$ kinematic viscosity, $\mu/\rho_L$
$\mu$ viscosity
$\xi$ curvilinear coordinate
$\rho$ density

* Corresponding author. Current address: Department of Chemical Engineering, National Taiwan University, Taipei, Taiwan 106, Republic of China. E-mail: lan@ruby.che.ntu.edu.tw

0017–9310/98 $19.00 
PII: S0017–9310(98)00119–7

$\sigma$ Stefan–Boltzmann constant
$\psi$ stream function
$\omega$ vorticity.

*Subscripts*
$a$ ampoule
$f$ feed
$c$ crystal
$L$ liquid or melt
m melt
max maximum
min minimum
$S$ solid.

## 1. Introduction

Modern electronics and communication are based on various devices in microscale, and the reliability of these devices is strongly affected by single crystal substrates. As it is, the homogeneity of the electrical (or optical) properties on microscale is required for device fabrication. It is well known that the convection in the melt during the production of these crystals can affect the crystal quality significantly. Particularly, unstable crystal growth conditions can lead to flow induced striation, and thus inhomogeneity, in the grown crystal. Accordingly, heat (mass) transfer and fluid flow during crystal growth have received considerable research attention in the past two decades. To control the crystal growth effectively, understanding of the process dynamics is necessary.

The vertical zone-melting (VZM) technique [1] is one of the most important processes for crystal growth and purification, i.e., zone refining. In the VZM process, crystal growth and zone-refining take place as the molten zone is traveled with a ring heater. Owing to the radial heating, strong buoyancy induced natural convection could be induced. Since the melt near the upper melt/solid interface is cooler, the unstable thermal convection may be of importance. Furthermore, accompanied by melting and solidification phenomena, the dynamic responses of the process to the changes on thermal environments could be very complicated.

Even though the VZM has been used to refine and to grow various single crystals for years [2–4], not many theoretical studies have been reported. Some of these studies are restricted to one-dimensional diffusion models [5, 6] in which heat transfer is neglected. There are only a few two-dimensional models [7–9] that calculated conductive thermal fields in the VZM crystal growth, but crystal growth and fluid flow were not considered. Recently, Apanovich and Ljumkis [10] simulated steady-state convective heat and mass transfer in the traveling solvent method (TSM) (a variant of VZM) for the crystal growth of a low Prandtl-number material, but the ampoule was neglected. Land and Yang [11] used a finite-volume/Newton method with an implementation of pseudo arc-length continuation to study the pseudo steady-state VZM growth of $NaNO_3$, in which multiple steady states were also observed. More interestingly, it was observed that the bifurcation of solutions is accompanied by the inversion of the upper interface. Lan and Yang also extended the simulation to the mass transfer and constitutional supercooling in the TSM growth of CdTe crystals from Te solution [12]. However, dynamic behavior of the VZM process has not yet been reported. Even though in most cases the process could achieve a pseudo steady-state very quickly after the crystal growth starts, at the initial stage of crystal growth and the onset of unstable convection, the process is still dynamic in nature. In other words, a pseudo steady-state model (PSSM) may not be adequate to describe the system.

The main purpose of this paper is to study the dynamic behavior of VZM crystal growth from various basic states. Time evolution of axisymmetric flow structures and growth rates will be illustrated through computer simulation. Some of the results may also give some explanations for the phenomena observed during crystal growth experiments. The VZM growth of $NaNO_3$ in a transparent multizone furnace [13] will be used as examples. Although unsteady-state three-dimensional flow were observed at some growth conditions in our crystal growth experiments, axisymmetric results could still be useful, and provide some conservative prediction of the instability. Moreover, since $NaNO_3$ is a high Prandtl-number material ($Pr = 9.2$), the interaction of thermal convection and interface shapes, which is interesting to us, is expected to be significant.

## 2. Mathematical formulation

The VZM growth of $NaNO_3$ single crystals is simulated using a transient model. If heating is axisymmetric, the physical domain for the feed, the melt zone, the crystal, and the ampoule can be taken as shown in Fig. 1. As it is, it may be treated as a two-dimensional model. It should be pointed out that three-dimensional flow was observed in some growth conditions. However, calculations of three-dimensional unsteady flow in this moving boundary problem are time consuming, and beyond the capability of present approach. The RHS of Fig. 1 shows an effective ambient temperature distribution for computation. During crystal growth experiments, this temperature distribution is assigned to the inner wall of the transparent furnace. The flow and temperature fields, as well as the shapes of the feed front (the feed/melt interface, $h_f(r, t)$) and the growth front (the melt/crystal interface, $h_c(r, t)$), are represented in cylindrical coordinate system $(r, z)$.

In this report, the melt is assumed incompressible and

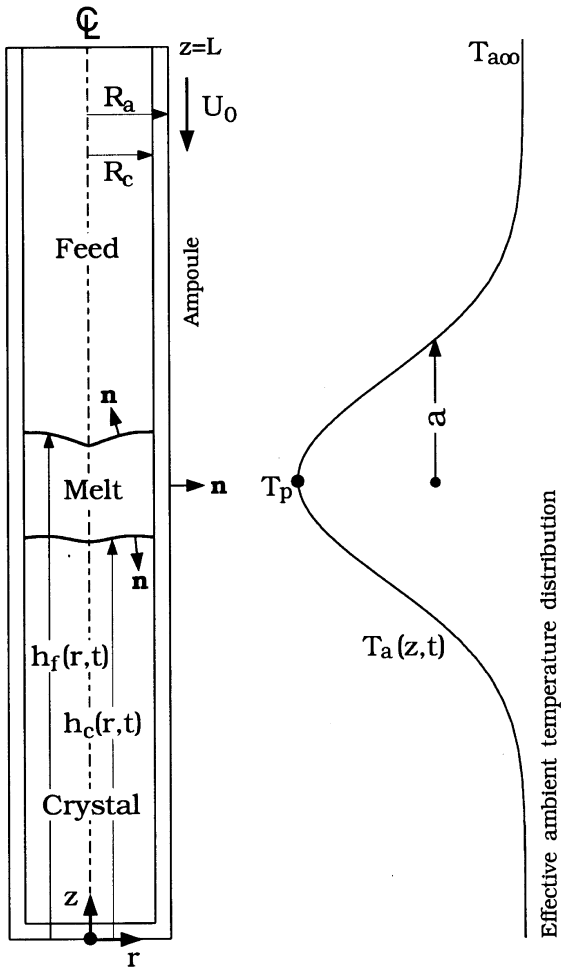


Fig. 1. Schematic sketch of the vertical zone-melting (VZM) crystal growth process; the RHS is an effective ambient temperature distribution.

Newtonian, while the flow is laminar. The Boussinesq approximation is also adopted. If the stream function $\psi$ and vorticity $\omega$ are defined in terms of radial ($u$) and axial ($v$) velocities as [14]:

$$u = -\frac{1}{\rho_L r}\frac{\partial \psi}{\partial z}, \quad v = \frac{1}{\rho_L r}\frac{\partial \psi}{\partial r} \tag{1}$$

and

$$\omega = \frac{\partial u}{\partial z} - \frac{\partial v}{\partial r} \tag{2}$$

the governing equations in the conservative-law form (or the so-called divergence form) for unsteady-state fluid flow and heat transfer in the system can be written as follows:

*Equation of motion*

$$-\rho_L \frac{\partial \omega}{\partial t} + \frac{\partial}{\partial r}\left(\frac{\omega}{r}\frac{\partial \psi}{\partial z}\right) - \frac{\partial}{\partial z}\left(\frac{\omega}{r}\frac{\partial \psi}{\partial r}\right) + \frac{\partial}{\partial r}\left(\frac{1}{r}\frac{\partial}{\partial r}(\mu r \omega)\right) + \frac{\partial}{\partial z}\left(\frac{1}{r}\frac{\partial}{\partial z}(\mu r \omega)\right) - \rho_L \beta_T g \frac{\partial T}{\partial r} = 0. \tag{3}$$

*Stream equation*

$$\frac{\partial}{\partial z}\left(\frac{1}{\rho_L r}\frac{\partial \psi}{\partial z}\right) + \frac{\partial}{\partial r}\left(\frac{1}{\rho_L r}\frac{\partial \psi}{\partial r}\right) + \omega = 0. \tag{4}$$

*Energy equation*

$$-\rho C_p r \frac{\partial T}{\partial t} - \frac{\partial}{\partial r}(\rho_i C_{pi} r u T) - \frac{\partial}{\partial z}(\rho_i C_{pi} r v T) + \frac{\partial}{\partial z}\left(r k_i \frac{\partial T}{\partial z}\right) + \frac{\partial}{\partial r}\left(r k_i \frac{\partial T}{\partial r}\right) = 0, \quad i = (L, S, a) \tag{5}$$

where $\mu$ is the viscosity, $\rho_i$ the density, $C_{pi}$ the specific heat, and $k_i$ the thermal conductivity of phase $i$; $i$ represents the melt ($L$), the crystal or feed ($S$), and the ampoule ($a$). Also $g$ is the gravitational acceleration and $\beta_T$ the thermal expansion coefficient of the melt. Also, the associated Rayleigh number $Ra$ can be defined as $\beta_T R_c^3 g(T_{max} - T_m)/(\nu\alpha)$, where $T_{max}$ is the maximum temperature in the zone, $T_m$ the melting point, $\nu = \mu/\rho_L$, and $\alpha = k_L/(\rho_L C_{pL})$. All the physical properties used in $Ra$ are obtained at $T_m$. Furthermore, since $T_{max}$ is unknown a priori, $Ra$ should be obtained from the solution.

The thermal boundary conditions are as follows:

(1) Along the centerline,

$$\partial T/\partial r = 0 \tag{6}$$

due to symmetry.

(2) At the feed (f) and crystal (c) growth fronts, the interfacial energy balance is

$$k(\mathbf{n}\cdot\nabla T)|_i - k(\mathbf{n}\cdot\nabla T)|_L + \rho_S \Delta H\left(\frac{\partial h_i}{\partial t} + U_0\right)\mathbf{n}\cdot\mathbf{e}_z = 0, \quad i = (f, c) \tag{7}$$

where $\mathbf{n}$ is the unit normal vector pointing into the feed or the crystal and $\Delta H$ the heat of fusion. The temperature at feed and growth fronts is set to the equilibrium melting point of the crystal:

$$T|_f = T|_c = T_m. \tag{8}$$

(3) At the material/ampoule interface, the energy balance is

$$k(\mathbf{n}\cdot\nabla T)|_i - k(\mathbf{n}\cdot\nabla T)|_a = 0, \quad i = (f, L, c) \tag{9}$$

where $\mathbf{n}$ is the unit normal vector pointing into the ampoule.

(4) Heat transfer from the system to the ambient is by both radiation and convection according to the energy balance along the ampoule surface:

$$-k_a(\mathbf{n}\cdot\nabla T) = h(T-T_a)+\varepsilon_a\sigma(T^4-T_a^4) \tag{10}$$

where $h$ is the heat transfer coefficient, $\varepsilon_a$ the thermal emissivity of the ampoule, $\sigma$ the Stefan–Boltzmann constant, and $T_a$ the effective ambient temperature.

(5) At the top of the sample, an adiabatic condition is used,

$$\mathbf{n}\cdot\nabla T = 0. \tag{11}$$

Heat loss from the top surface can be added if necessary.

Heat exchanges between the surrounding (furnace) and the ampoule are dictated by the effective ambient temperature $T_a(z)$ specified along the zone length. The effective ambient temperature distribution due to the furnace is specified as follows:

$$T_a(z,t) = (T_p-T_{a\infty})\exp\{-[(z-z_p)/a]^2\}+T_{a\infty} \tag{12}$$

and

$$z_p = z_{p0}+U_{heater} \tag{13}$$

where $T_p$ and $T_{a\infty}$ are the peak and background temperatures, respectively, the parameter $a$ is related to the width of the distribution, and $z_p$ is the position of $T_p$. Also, $z_{p0}$ is the initial position of $T_p$. The heating profile according to equation (12) can be generated in the computer-controlled multizone furnace easily [13].

The fluid-flow boundary conditions are as follows:

(1) Along the centerline

$$\psi = 0, \quad \omega = 0 \tag{14}$$

where $\psi$ is set to zero as a reference.

(2) At the feed and growth fronts,

$$\psi = \tfrac{1}{2}\rho_S U_0 r^2$$

$$\omega = \frac{\partial u}{\partial z}-\frac{\partial v}{\partial r} \tag{15}$$

with

$$u = 0, \quad v = U_0\rho_S/\rho_L. \tag{16}$$

Also, $U_0$ is negative here if the ampoule is pulled downwards.

(3) At the melt/ampoule interface,

$$\psi = \frac{1}{2}\rho_S U_0 R_c^2, \quad \omega = \frac{\partial u}{\partial z}-\frac{\partial v}{\partial r} \tag{17}$$

with

$$u = 0, \quad v = U_0\rho_S/\rho_L \tag{18}$$

where $R_c$ is the crystal radius (see Fig. 1).

## 3. Solution procedure

The above governing equations and boundary conditions are transformed into those in terms of general (nonorthogonal) curvilinear coordinates $(\eta,\xi)$ which fit all the interfaces, as shown in Fig. 2. In this way, all the boundary conditions can be treated accurately, as already described previously [15].

The equation of motion, the stream equation, and the energy equation [equations (3)–(5)] are discretized by employing a finite-volume method. The physical domain, in $(r,z)$, is subdivided into a finite number of contiguous volumes (CVs) of volume $V$, which are bounded by cell faces located about halfway between consecutive nodal points. For any CV with volume $V$ in this domain can be transformed into a computation domain $(\eta,\xi)$ with a CV of volume $V'$, and $\mathrm{d}V = J\,\mathrm{d}V'$, where $J$ is the Jacobian of coordinate transformation ($J = r_\eta z_\xi - r_\xi z_\eta$). Now, the integration of these equations over the CV can proceed as follows:

$$\int_V [\text{equations (3)–(5)}]\,\mathrm{d}V. \tag{18}$$

After the Gauss theorem is applied, the above equation can be transformed into surface integrals (fluxes) over the surface of the CV. The resulting balance equations for each CV can then be expressed as

$$I_{east}-I_{west}+I_{north}-I_{south}+\int_{V'}\left(-b'\frac{\partial\phi}{\partial t}\bigg|_{r,z}+d\right)J\,\mathrm{d}\eta\,\mathrm{d}\xi = 0 \tag{19}$$

and

$$\frac{\partial\phi}{\partial t}\bigg|_{r,z} = \frac{\partial\phi}{\partial t}\bigg|_{\eta,\xi}+\frac{1}{J}\left[(r_\xi\phi_\eta-r_\eta\phi_\xi)\left(\frac{\partial z}{\partial t}\bigg|_{\eta,\xi}\right)-(z_\xi\phi_\eta-z_\eta\phi_\xi)\left(\frac{\partial r}{\partial t}\bigg|_{\eta,\xi}\right)\right] \tag{20}$$

where $\phi$ is the field variables (i.e., $\omega$, $\psi$, and $T$), $d$ the source terms in the governing equations, $b'$ the corresponding coefficient for time derivative of $\phi$, and $I_i$ represents the total flux of $\phi$ across the face $i$ of the CV. The second term on the RHS of equation (20) is due to the moving coordinate in the physical domain. Equation (19) involves no approximation and represents the finite-volume equations of the differential equations. Numerical evaluation of the different terms in equation (19) requires the calculation of geometrical factors for the CVs and a discretization scheme for interpolating quantities at

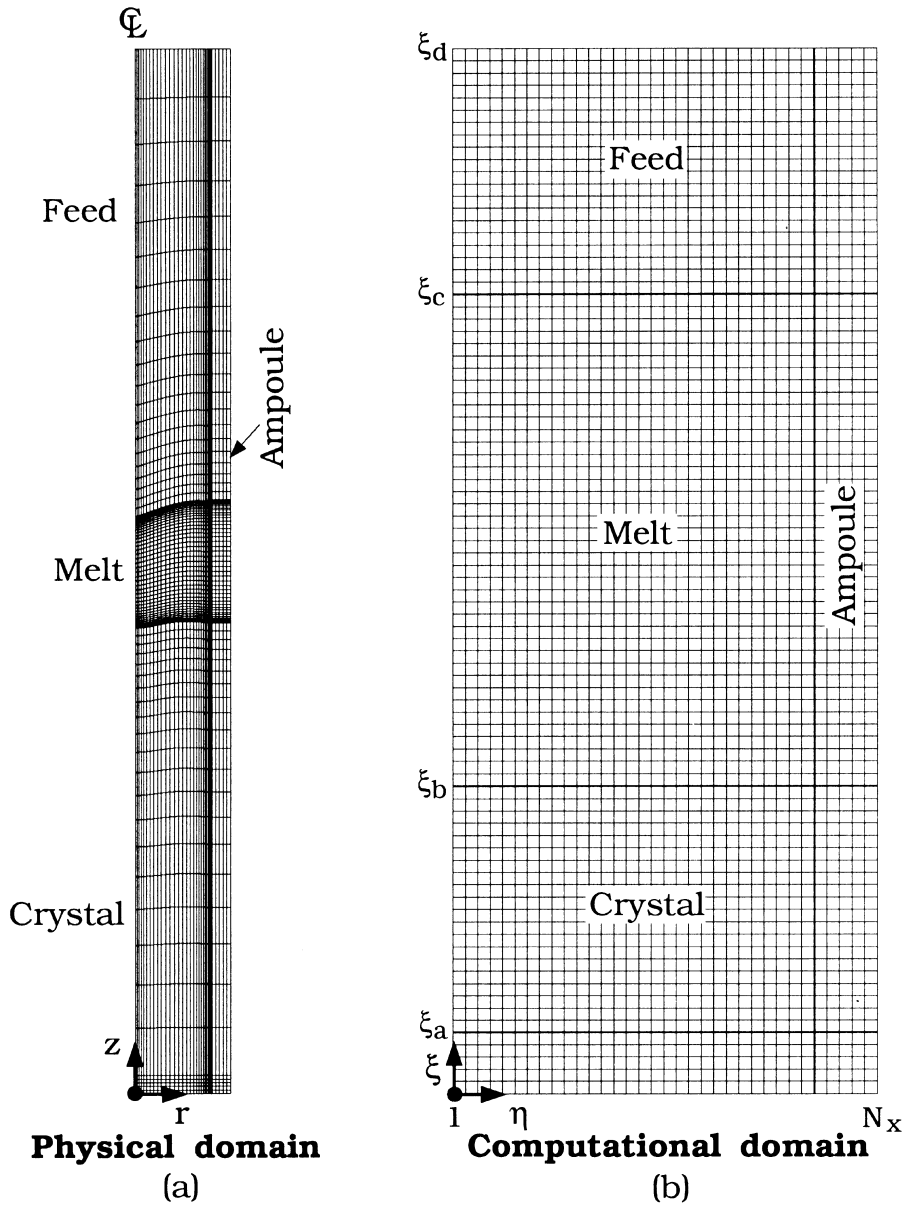


Fig. 2. A nonorthogonal body-fitted coordinate system used for computation: (a) physical domain; (b) computational domain. The heavy lines indicate the interfaces in the computational domain.

the cell faces from their adjacent nodal values. The details of the discretization scheme can be found elsewhere [15]. In addition, the boundary conditions are discretized by second order finite differences.

After the discretization for both governing and boundary conditions, a set of differential/algebraic equations (DAEs) can be obtained:

$$\mathbf{f}\left(\mathbf{x}, \frac{\mathrm{d}\mathbf{x}}{\mathrm{d}t}, t\right) = 0 \tag{21}$$

where $\mathbf{x}^{\mathrm{T}} = (\psi, \omega, T, h_f, h_c)$. The formulation of the DAEs is then completed by specifying an initial condition ($t = 0$) on the stream function, vorticity, temperature, and the interface shapes. The solution at a stationary state, in which the ampoule and the ambient temperature profile are both kept stationary, is taken as the initial condition. The stationary state is solved by Newton's method, and the detailed description can be found elsewhere [11]. To solve the DAEs, a fully implicit time integration code DASPK [16] (a variant of DASSL [17]) is

used. In the DASPK code, nonlinear equations involved in each time step are solved by an inexact Newton method based on the Krylov subspace iterative approach [18]. The incomplete $LU$ decomposition without fill-in ($ILU(0)$) [19] of the Jacobian matrix from equation (21) is used as the preconditioner during inexact Newton's iterations. The components of the Jacobian matrix $\tilde{J}$, formed by explicit differentiation as $\tilde{J}_{ij} \equiv \partial f_i/\partial x_j$, represent the sensitivity of the residual vector to the solution vector, and are obtained by finite-difference approximations with the consideration of the sparse structure of $J$ [20]. Since the Krylov subspace method is adopted in the solution phase, the choice of the preconditioner is crucial to the success of DASPK. In addition, the consistence of the initial condition is also sensitive to this DAE solver.

## 4. Results and discussion

The calculated results are based on the physical properties and some input parameters in Table 1. According to the table, the Prandtl number ($Pr = \mu C_{pL}/k_L$) for $NaNO_3$ is rather high, i.e., around 9.2 at the melting point (306.8°C). Before calculated results are presented, mesh refinements are also performed to examine discretization errors. Two meshes are tested in the study. The coarser mesh has $26 \times 76$ grid points, which leads to totally 3190 nonlinear equations. The finer mesh, as shown in Fig. 2, has $36 \times 86$ grid points and has up to 5520 nonlinear equations. In details, the grids are $31 \times 21$ in the feed, $31 \times 41$ in the melt, $31 \times 21$ in the crystal, and the rest of grids in the ampoule. Calculated results (flow patterns, isotherms, and the growth rate curve) for a case under normal gravity ($T_p = 350$°C and $U_{heater} = 1$ cm h$^{-1}$) based on the two meshes are very close to each other (the difference on the maximum of temperature is within 1%). Since a calculation with the finer mesh (if the system is stable) takes only about 30 CPU minutes in HP9000/735 workstation, the finer mesh is chosen for all the calculations here.

Table 1
Physical properties and some input parameters [11]

$NaNO_3$
- $T_m = 306.8$°C
- $\Delta H = 182$ J g$^{-1}$
- $k_s = 5.65 \times 10^{-3} + 33.5(T-230) \times 10^{-7}$ W cm$^{-1}$ °C$^{-1}$
- $k_L = 5.65 \times 10^{-3} + 44.7(T-T_m) \times 10^{-7}$ W cm$^{-1}$ °C$^{-1}$
- $C_{p_s} = C_{p_L} = 1.255 + 2.18(T-100) \times 10^{-3}$ J g$^{-1}$ °C$^{-1}$
- $\mu = 0.0302 - 1.533 \times 10^{-4}(T-T_m)$ g cm$^{-1}$ s$^{-1}$
- $\beta_T = 6.6 \times 10^{-4}$ °C$^{-1}$
- $\rho_S = 2.118$ g cm$^{-3}$
- $\varepsilon_L = 1.904$ g cm$^{-3}$

Ampoule (glass)
- $k_a = 0.035$ W cm$^{-1}$ °C$^{-1}$
- $C_{p_a} = 0.188$ J g$^{-1}$ °C$^{-1}$
- $\rho_a = 2.2$ g cm$^{-3}$
- $\varepsilon_a = 0.7$

Some input parameters
- $R_c = 0.725$ cm
- $R_a = 0.9$ cm
- $L = 10$ cm
- $z_{p0} = 5.1$ cm
- $T_p = 350$ or 380°C
- $T_{a\infty} = 180$°C
- $a = 1.6$ cm
- $h = 1.6 \times 10^{-2}$ W cm$^{-2}$ °C$^{-1}$
- $U_0 = 0$ cm h$^{-1}$
- $U_{heater} = 1$ cm h$^{-1}$

Before transient results are presented, the initial conditions are discussed first. Figure 3 shows the variation of zone length (measured at the centerline) with the gravity level; the solutions from the pseudo steady-state model (PSSM) [11] is indicated by the dashed-line. As shown, the zone length increases rapidly with the increasing gravity. Since the gravity is the only driving force for convection in the melt, Fig. 3 can be seen as the effect of convection on the molten zone size. More interestingly, there are multiple steady states near the gravity level around 0.08 $g$. The corresponding flow patterns and isotherms are also illustrated; the upper flow cell is anticlockwise while the lower one is clockwise in direction. The values for the maximum temperature ($T_{max}$), maximum ($\psi_{max}$) and minimum ($\psi_{min}$) stream functions are listed in Table 2. The associated $Ra$ number is also included for reference. In fact, as discussed in the previous report [11], the bifurcation is accompanied by the inversion of the upper melt/solid interface. Similar bifurcation behavior can be found in Czochralski crystal growth [21], in which the cold boundary (the melt/crystal interface) is on the top. We have also conducted the calculations for the cases with 'fixed' interfaces. However, no similar bifurcation behavior is observed. Since the dynamic response of the multiple steady states to the change of thermal environments could be interesting, solutions (or the so-called basic states) a–c in Fig. 3 are chosen as initial conditions.

The dynamic response of the basic states a–c is illustrated first for a pulse disturbance. The disturbance is implemented through a pulse increase on the peak heater temperature ($T_p(t) = T_p(0) + 5\sin(t)$ for $t \leqslant \pi$). The dynamic response of zone length for the basic states a–c is shown in Fig. 4. As shown, the basic state c still remains at its original state, and is not affected by the disturbance much. On the contrary, for the states a and b, they do not stay at their original states, and their zone length is changing with time until a new steady state is reached. Interestingly, the new stable state appears to be the basic

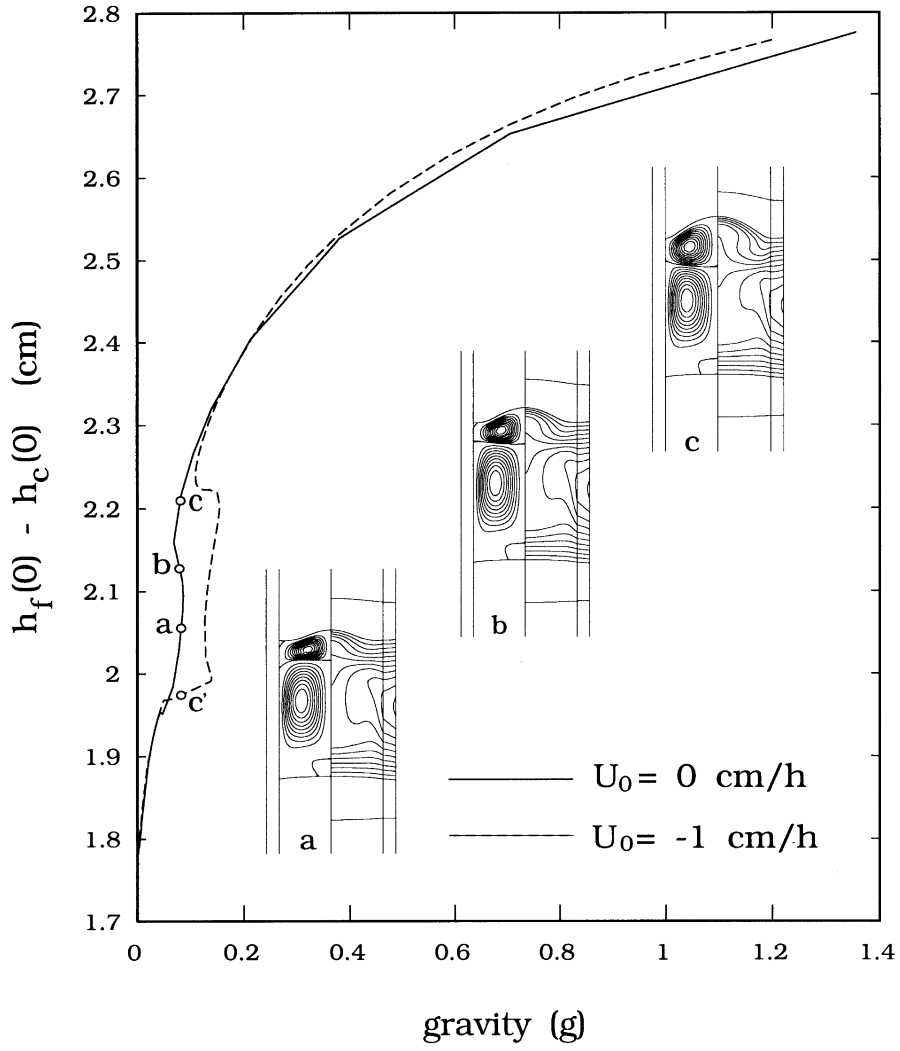


Fig. 3. Effect of gravity levels on the zone length; $T_p = 380°C$.

state c. More importantly, the response of the growth rate (Fig. 5) are oscillatory for both states a and b. In fact, the cyclic melting ($dh_c/dt < 0$) and growth ($dh_c/dt > 0$) could be responsible to the striation during crystal growth. Although the amplitude of the oscillation for both basic states a and b decays to zero eventually, the oscillation can sustain up to 400 s. The detailed response of the growth rate at the first 100 s is also highlighted in the same figure. It can be clearly seen that the growth rate for the state c is not oscillatory at all, and it returns to zero in 20 s. The *Ra* for all of the cases is about $1.8 \times 10^5$, which is much smaller than the critical *Ra* ($\approx 1 \times 10^7$) reported for the simulated VZM system using water as a model fluid [22]. The response of a basic state at higher *Ra* in Fig. 3 is similar to the basic state c.

The dynamic response of these basic states to the step change of the heater moving speed (to start up crystal growth) may also be interesting; $U_{heater}$ is changed from 0 to 1 cm $h^{-1}$ upwards. Figure 6 shows the response of the growth rate for the state a. As shown, the system does not respond until the change in the thermal environments is substantial. Interestingly, as the system senses the change, the response, for both the growth rate and the flow patterns, is oscillatory with time periodically. The oscillation pattern is similar to that in Fig. 5. From the associated flow patterns and isotherms indicated from points b–f (a period), it is clear that the periodic growth or melting is mainly due to the oscillatory flow. From the flow patterns, it can be seen that the upper flow cell moves back and forth horizontally from b–f, and the lower cell is induced to move up and down. The unstable upper cell, presumably, may be due to the unstable thermal

Table 2
Calculated stream function, and *Ra*

| Figures | $\Psi_{min}$ ($\times 10^2$) [g s$^{-1}$] | $\Psi_{max}$ ($\times 10^3$) [g s$^{-1}$] | $T_{max}$ [°C] | $Ra$ ($\times 10^{-5}$) |
|---|---|---|---|---|
| Fig. 3a | −1.78 | 3.13 | 345.17 | 1.813 |
| Fig. 3b | −1.89 | 5.34 | 344.82 | 1.797 |
| Fig. 3c | −1.85 | 11.8 | 344.41 | 1.778 |
| Fig. 6b | −1.99 | 4.27 | 344.65 | 1.789 |
| Fig. 6c | −2.42 | 1.92 | 344.24 | 1.769 |
| Fig. 6d | −2.22 | 0.51 | 344.51 | 1.782 |
| Fig. 6e | −1.35 | 11.5 | 344.39 | 1.776 |
| Fig. 6f | −1.98 | 4.16 | 344.61 | 1.787 |
| Fig. 7b | −1.71 | 1.07 | 345.17 | 2.043 |
| Fig. 7c | −2.01 | 4.70 | 344.60 | 1.786 |
| Fig. 7d | −1.52 | 9.71 | 344.67 | 1.790 |
| Fig. 7e | −1.74 | 10.0 | 345.00 | 1.805 |
| Fig. 8b | −1.58 | 3.24 | 344.82 | 1.834 |
| Fig. 8c | −1.58 | 3.23 | 345.62 | 1.835 |
| Fig. 9a | −2.24 | 0.02 | 320.47 | 0.194 |
| Fig. 9b | −2.91 | 0.42 | 320.24 | 0.381 |
| Fig. 9c | −2.83 | 1.90 | 320.37 | 0.641 |
| Fig. 10b | −3.15 | 1.08 | 320.20 | 0.633 |
| Fig. 10c | −3.57 | 0.27 | 320.10 | 0.629 |
| Fig. 12a | −3.32 | 4.00 | 325.41 | 0.879 |
| Fig. 12b | −3.46 | 4.09 | 325.29 | 0.873 |
| Fig. 12c | −4.13 | 10.6 | 324.83 | 0.852 |
| Fig. 15b | −4.08 | 4.12 | 324.36 | 0.830 |
| Fig. 15c | −3.29 | 9.50 | 324.52 | 0.837 |
| Fig. 15d | −4.04 | 4.40 | 324.26 | 0.825 |
| Fig. 15e | −3.29 | 9.56 | 324.48 | 0.836 |
| Fig. 16b | −4.14 | 5.28 | 324.37 | 0.830 |
| Fig. 16c | −3.35 | 10.0 | 324.56 | 0.839 |
| Fig. 16d | −4.10 | 5.52 | 324.29 | 0.827 |
| Fig. 16e | −3.35 | 10.1 | 324.52 | 0.837 |
| Fig. 17b | −4.34 | 7.79 | 324.28 | 0.826 |
| Fig. 17c | −3.65 | 17.2 | 324.54 | 0.838 |
| Fig. 17d | −4.31 | 8.22 | 324.26 | 0.825 |
| Fig. 17e | −3.67 | 17.0 | 324.53 | 0.838 |

configuration; the cold boundary (the feed front) is on the top. Isotherm variation due to the flow is also very obvious. However, due to the short growth time, the change on the interfaces are invisible. Since the heater is moved upward, the mean growth rate should increase upwards as well; $dh_c/dt = U_{heater}$ if a steady state is achieved. Unfortunately, due to the oscillatory behavior while we need to maintain the accuracy of the solution at each time step, we were not able to obtain a steady-state solution in a reasonable CPU time. Again, the dynamic response of the basic state b also exhibits a similar behavior (Fig. 7), but as is the case in Fig. 5 the amplitude of the periodic oscillation is smaller. Furthermore, the upper cell now moves up and down rather than left and right. The period for both cases a and b is about 6.8 s. On the contrary, the basic state c is stable, and the oscillatory behavior does not exist. As shown in Fig. 8, the system achieves a steady state smoothly. The feed front changes from concave to flat, while the growth front from slightly convex to concave. Furthermore, the new state c at Fig. 8 is consistent with the solution from a PSSM (point c′ in Fig. 3). In fact, since the basic state c′ in Fig. 3 is a unique stable solution at the growth rate of 1 cm h$^{-1}$, we anticipate that it may also be the final steady state for the basic states a and b to the step change on $U_{heater}$.

When the molten zone is short at a lower heater temperature ($T_p = 350$°C), no bifurcation occurs with the increasing gravity (Fig. 9). In fact, the *Ra* for the cases in Fig. 9 is less than $1 \times 10^5$ (see Table 2). The step response of the basic state c (at 1 *g*) is shown in Fig. 10. Again, since it is stable, a steady state is smoothly achieved, in which $dh_c/dt = U_{heater}$. Interestingly, an inverse response of the growth rate (from points a to b in Fig. 10) is observed. Indeed, in such a complicated system there are many associated time constants and their values may vary significantly. For example, the time constant for heat conduction is quite different from that for fluid flow. Therefore, as the heater moves upwards, the faster mode (convective heat transfer) tends to melt back the growth front (negative $dh_c/dt$). However, as the heater moves upwards more, the slower mode (heat conduction) can then respond more significantly to exhibit the positive growth rate. Figure 11 gives a simple comparison of the steady state results from Fig. 10 and the PSSM [11]. As shown, the PSSM is a good approximation to the system. The smaller difference in the stream function is simply due to the different boundary conditions used. Furthermore, the calculated flow patterns and interface shapes shown in Fig. 11 are also compared with those from the laser light-cut technique, and they are in good agreement. The detailed comparison is discussed elsewhere [13].

Similar bifurcation behavior can also be obtained by tracking the solution family using $T_p$ as a parameter. As shown in Fig. 12, under normal gravity condition multiple steady states also appear for both stationary and growth cases around $T_p = 1.085T_m$. Also, the bifurcation structure is more complicated, and there are four turning points [23]. The zone length for both stationary and growth cases are very close to each other for a wide range of $T_p$ except for the range with multiple steady states. The flow patterns and isotherms for multiple steady states at $T_p = 1.085T_m$ (labeled by a–c) are also illustrated. The basic state at a′ is the same as that at c in Fig. 9. Again, the major difference in these basic states is in the upper flow cell and interface. With a pulse disturbance on $T_p$, the dynamic response of zone length for these basic states is demonstrated in Fig. 13. Apparently, none of them is stable; at least no steady state can be achieved within 400 s. Much longer integration time may require to examine the stability of these states. Again, we were unable to

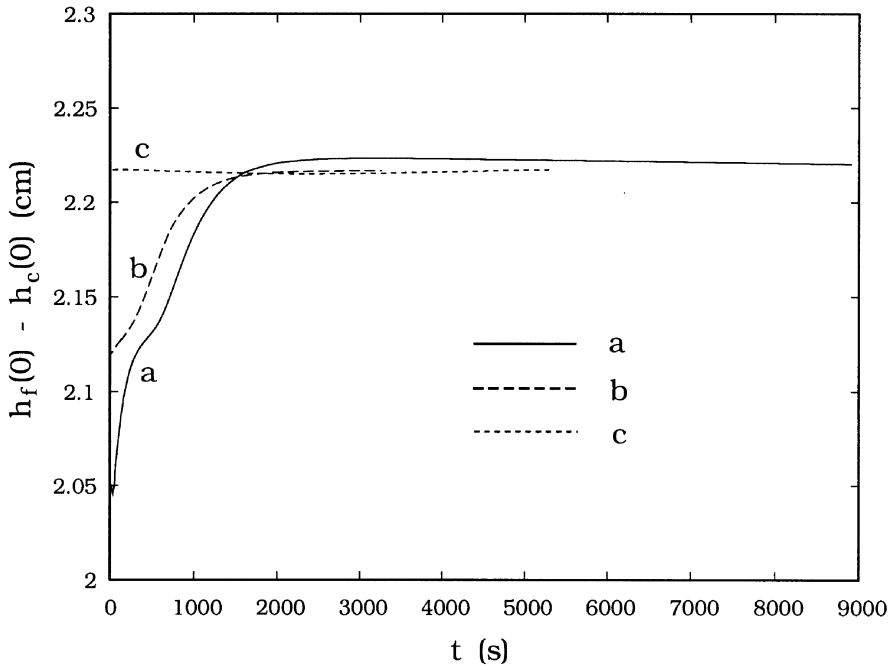


Fig. 4. Dynamic response of the zone length to the pulse change on the heater temperature. The initial conditions are from the basic states of Fig. 3.

obtain a steady state in a reasonable CPU time. The reason is explained in Fig. 14. As illustrated in Fig. 14 the growth rate for all the cases is oscillatory periodically with time, and its amplitude does not decay to zero. Due to the oscillatory nature, the step size for integration needs to be small for accuracy. In fact, more than 30 000 time steps (variable step size) are required for all the cases in Fig. 14. It should be pointed out that there may be stability changes between a′ and a, as well as c and c′ (stable) in Fig. 12. One way to monitor the stability changes, based on the linear stability theory, is to monitor the sign change of the determinant of the Jacobian during Newton's iterations [24]. However, this approach may fail when a Hopf bifurcation occurs. Furthermore, the linear stability theorem can only be applied for an infinitesimal disturbance. For a finite disturbance, the stability could be difficult to examine. Furthermore, in the present cases even if some of the states may be stable, they are still very easy to be excited by any thermal environment changes. In other words, striation in the grown crystal can be easily induced. During crystal growth experiments, it is observed that the flow and interfaces are not stable when the upper interface is nearly flat. In such a case the upper flow cells are much more unstable, and can easily move up and down or left and right periodically. This is consistent with the calculated results. Unfortunately, three-dimensional flow is always observed during crystal growth experiments when the flow is unstable. Furthermore, it is still not clear yet whether the three-dimensional periodic flow is due to asymmetrical heating or inherent flow instability.

The response of the growth rate for these basic states to the step change of $U_{\text{heater}}$ is also very interesting. As shown in Figs 15–17, the growth rate is also oscillatory periodically. For all of the cases, the upper flow cell (from points b–e) is moving back and forth horizontally; the period is about 2.3 s. Again, since the integration time is less than 25 s, the final states of these responses are still unknown. Nevertheless, the oscillatory flow patterns and growth rate indicate that the oscillatory features of the basic states a–c can be excited easily. Finally, it should be pointed out that the basic state c′ in Fig. 12 is stable, and it could achieve a steady state smoothly when the same disturbance is imposed, even though its zone length and associated *Ra* are much larger. In other words, in the present system, a less stable basic state does not need to have a high *Ra*. Muller and Neumann [25, 26] also observed similar phenomena in their horizontal zone melting experiments of InSb. Flow (temperature) oscillation were observed for intermediate values of the Rayleigh number.

## 5. Conclusions

(1) A fully transient model, which simulates axisymmetric unsteady-state fluid flow, heat transfer,

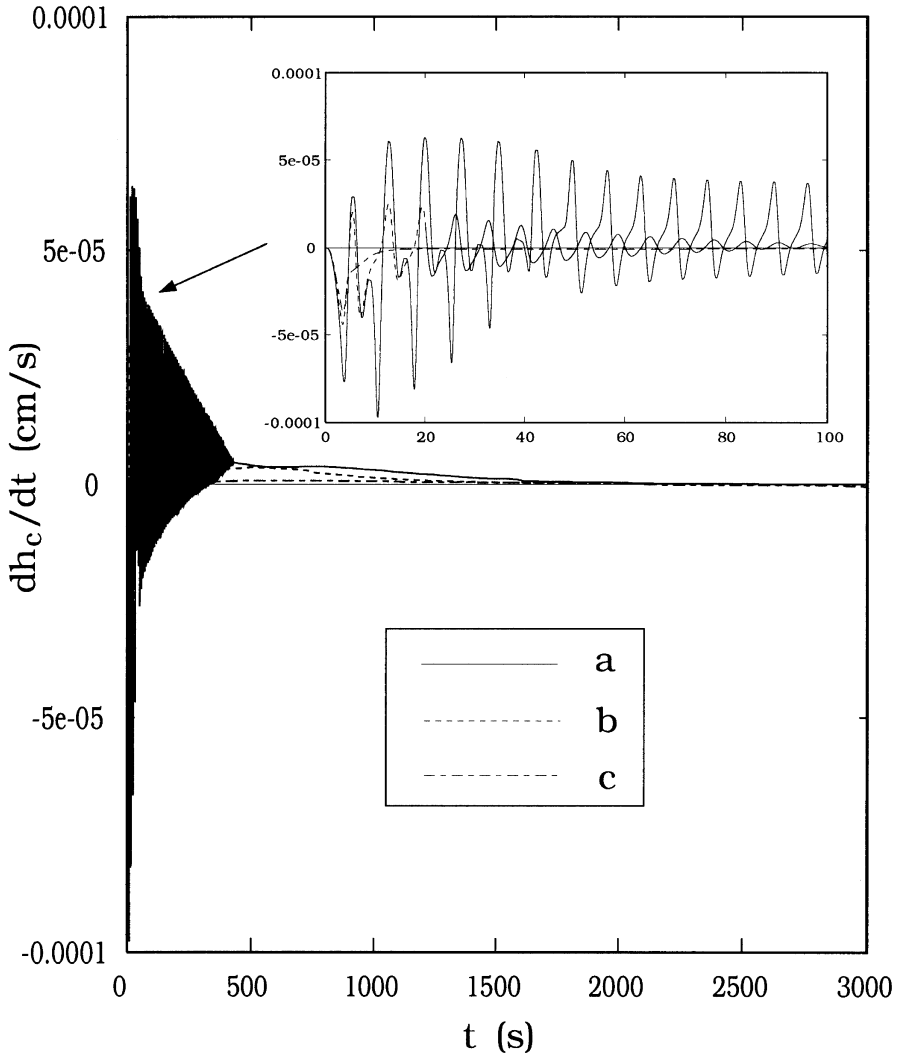


Fig. 5. Dynamic response of the growth rate to the pulse change on the heater temperature. The initial conditions are from the basic states of Fig. 3.

and interface shapes simultaneously, is used to study the dynamic behavior of the vertical zone-melting growth of $NaNO_3$ crystals. A finite-volume/Newton method with an implementation of the pseudo arclength continuation is used to obtain initial basic states for time integration. The integration of the differential/algebraic equations resulted from the finite-volume formulation is accomplished by *ILU*(0) preconditioned DASPK solver. The pulse disturbance of the peak heater temperature and the step change of the heater moving speed are both considered.

(2) When the system is studied using the gravity as a parameter, the stability of the basic states obtained from the same solution family can be examined by a pulse input of the peak heater temperature. For the stable case, the system could remain at its original state. On the contrary, for unstable cases, the system could run away from their original states, and eventually approach to the stable basic state. More interestingly, for the unstable basic states, the dynamic response of the flow and the growth rate to the pulse or the step disturbance is oscillatory periodically. Furthermore, the upper flow cells seem to be more unstable due to the unstable thermal configuration. This is consistent with the observation during crystal growth experiments.

(3) For a shorter zone at a lower heater temperature, no

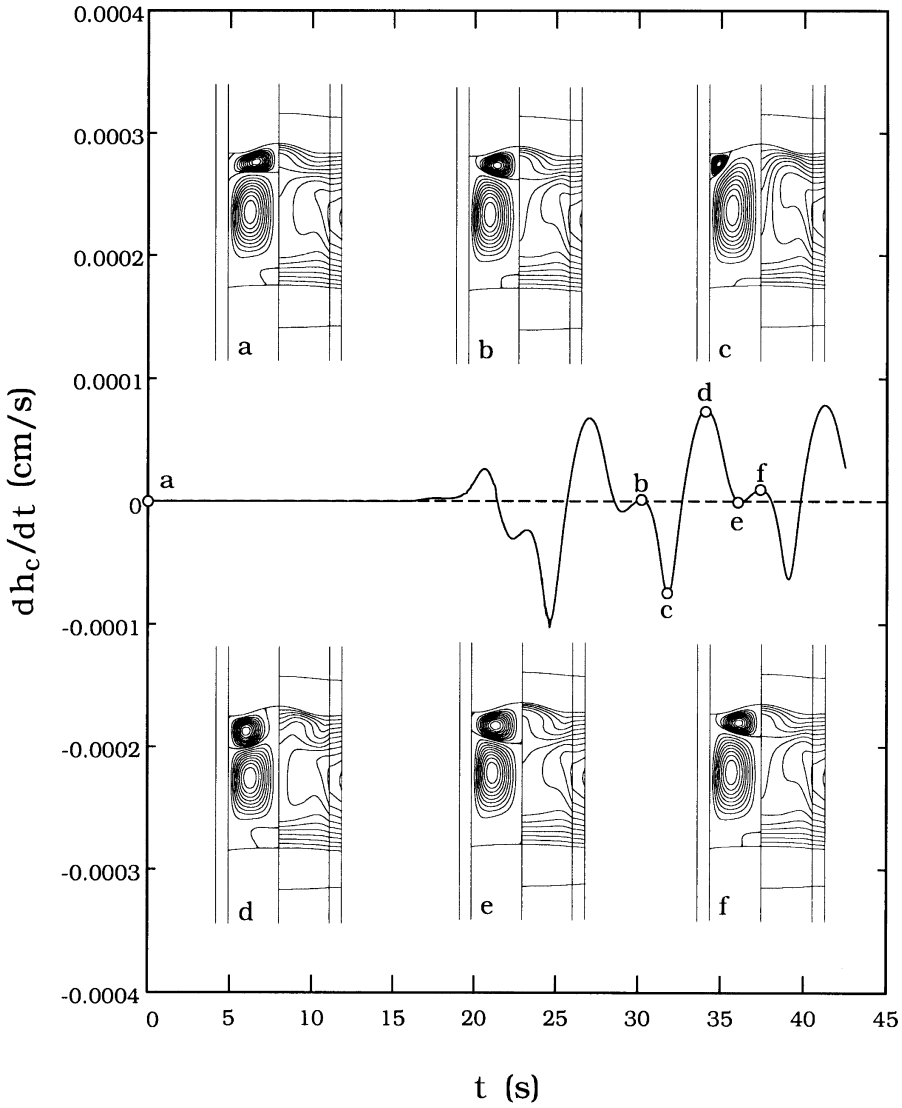


Fig. 6. Dynamic response of the growth rate and the associated flow patterns and isotherms of the basic state a of Fig. 3 to the step change on the heater moving speed $U_{heater}$.

bifurcation is observed. For such a case, the system is quite stable, and a new steady state can be achieved smoothly when a step change on the heater moving speed is applied. The new steady state can be approximated by the pseudo steady-state model very well.

(4) Similar bifurcation also exists when the solution family is tracked using the peak heater temperature as the parameter. However, for the basic states chosen, none of them is stable in this study. The flow patterns and the growth rates are all changing with time periodically. The oscillatory flow only occurs at intermediate values of the Rayleigh number in this study. The flow is stable at a smaller or a larger Rayleigh number.

## Acknowledgments

The authors are grateful for the support of National Science Council of ROC under Grant No. NSC82-402-E008-170. C.W.L. also acknowledges Dr Alan C. Hindmarsh of the Lawrence Livermore National Laboratory for fruitful discussions.

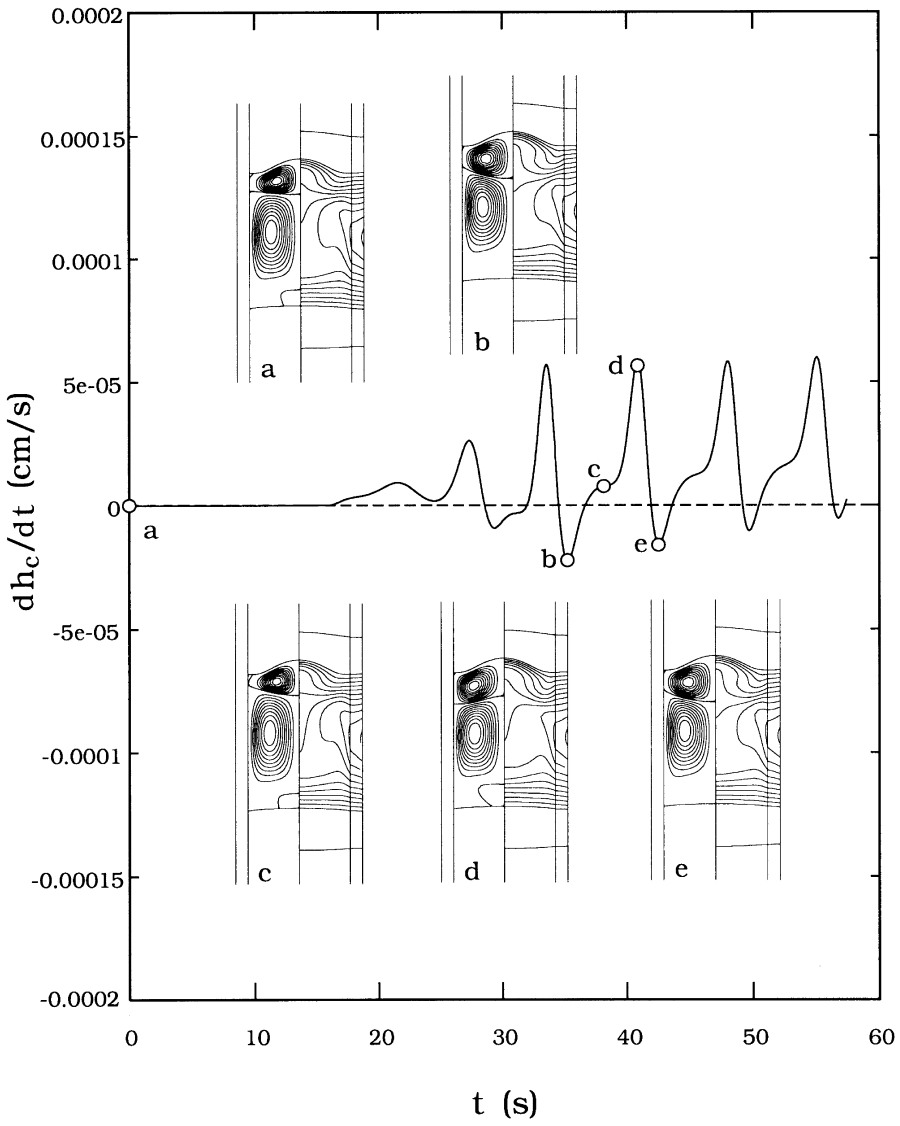


Fig. 7. Dynamic response of the growth rate and the associated flow patterns and isotherms of the basic state b of Fig. 3 to the step change on the heater moving speed $U_{heater}$.

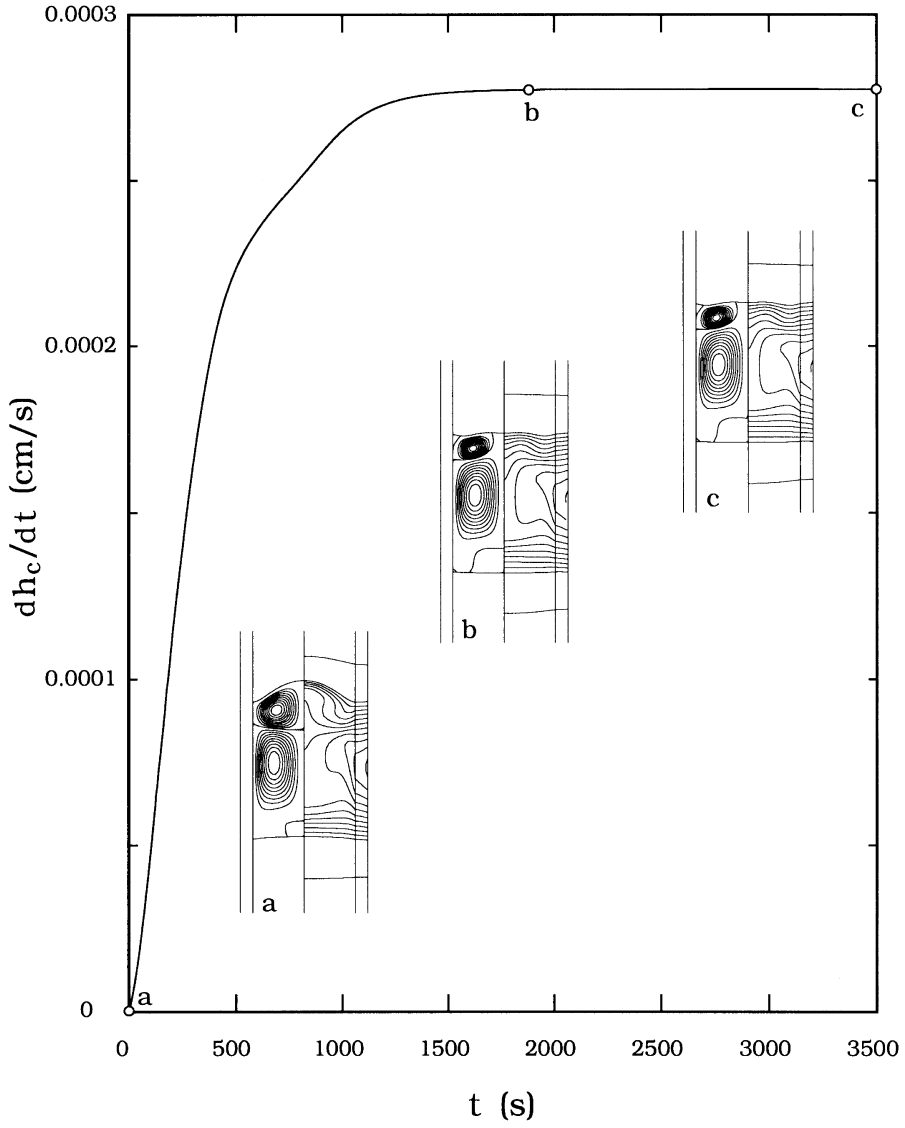


Fig. 8. Dynamic response of the growth rate and the associated flow patterns and isotherms of the basic state c of Fig. 3 to the step change on the heater moving speed $U_{\text{heater}}$.

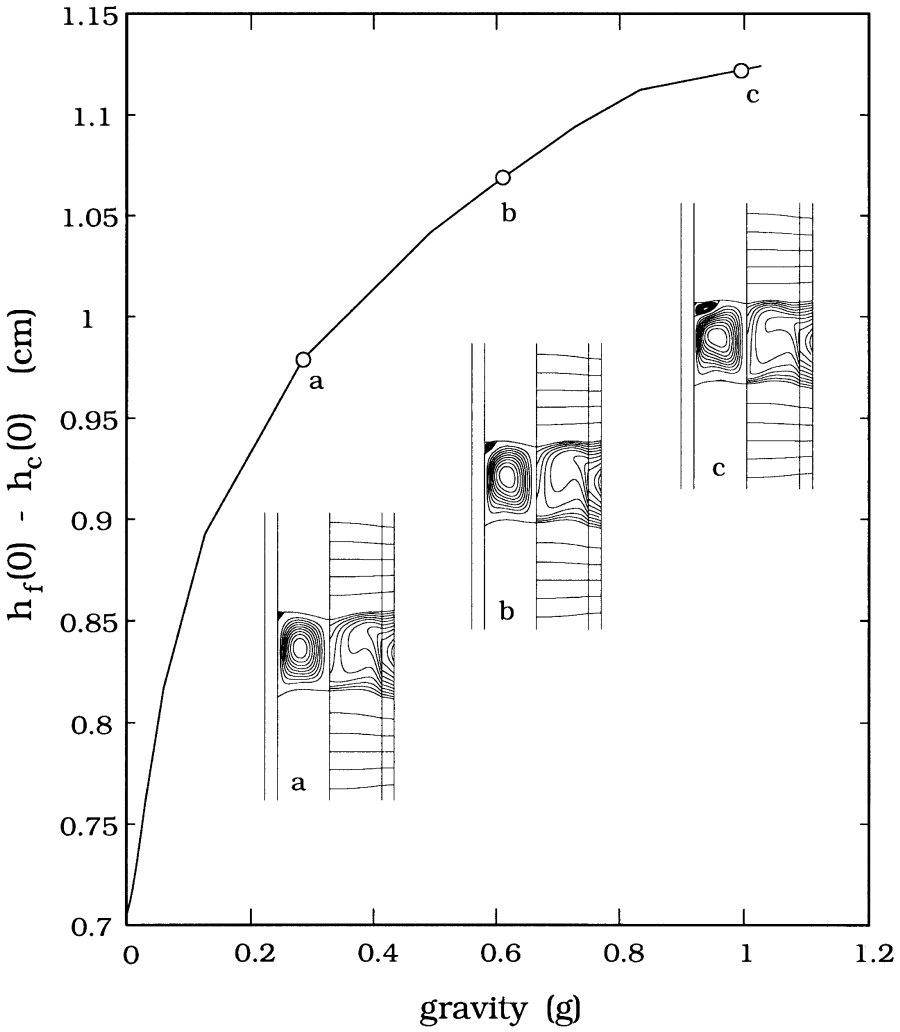


Fig. 9. Effect of gravity levels on the zone length; $T_p = 350°C$.

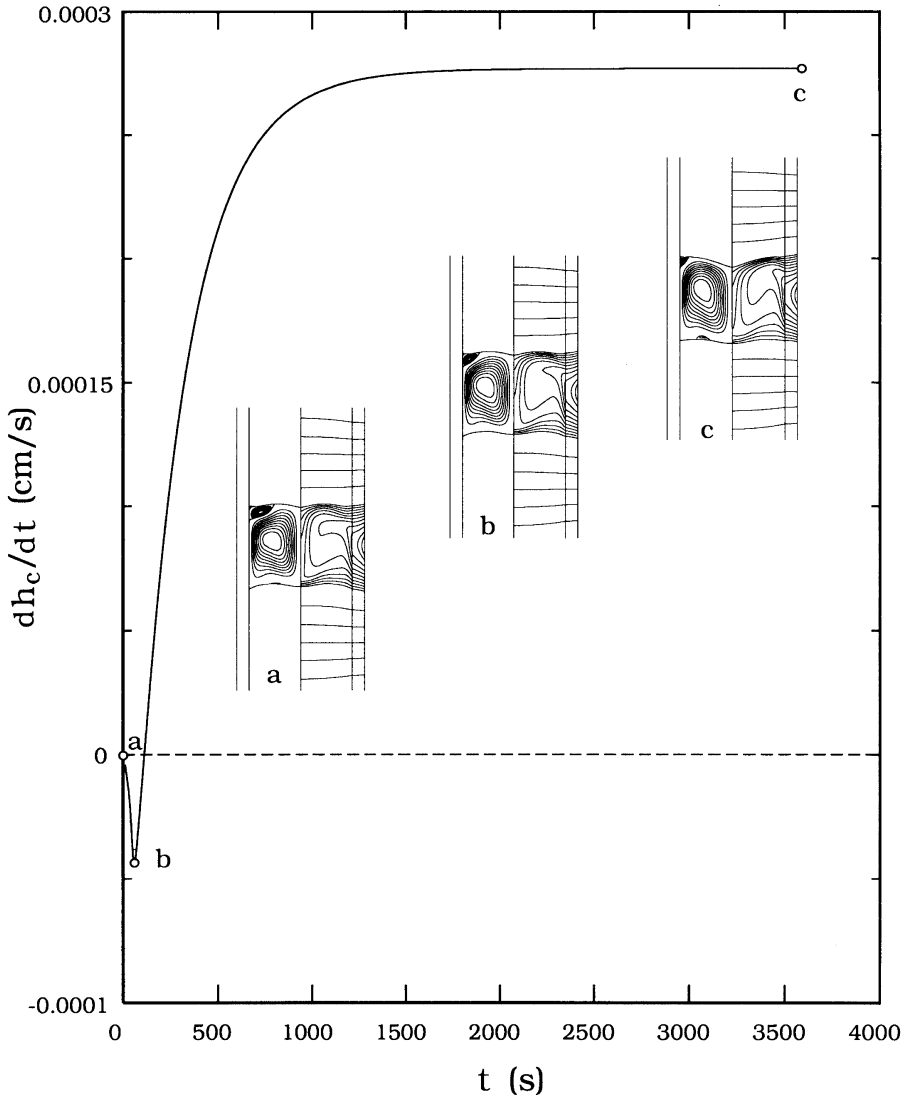


Fig. 10. Dynamic response of the growth rate and the associated flow patterns and isotherms of the basic state c of Fig. 9 to the step change on the heater moving speed $U_{heater}$.

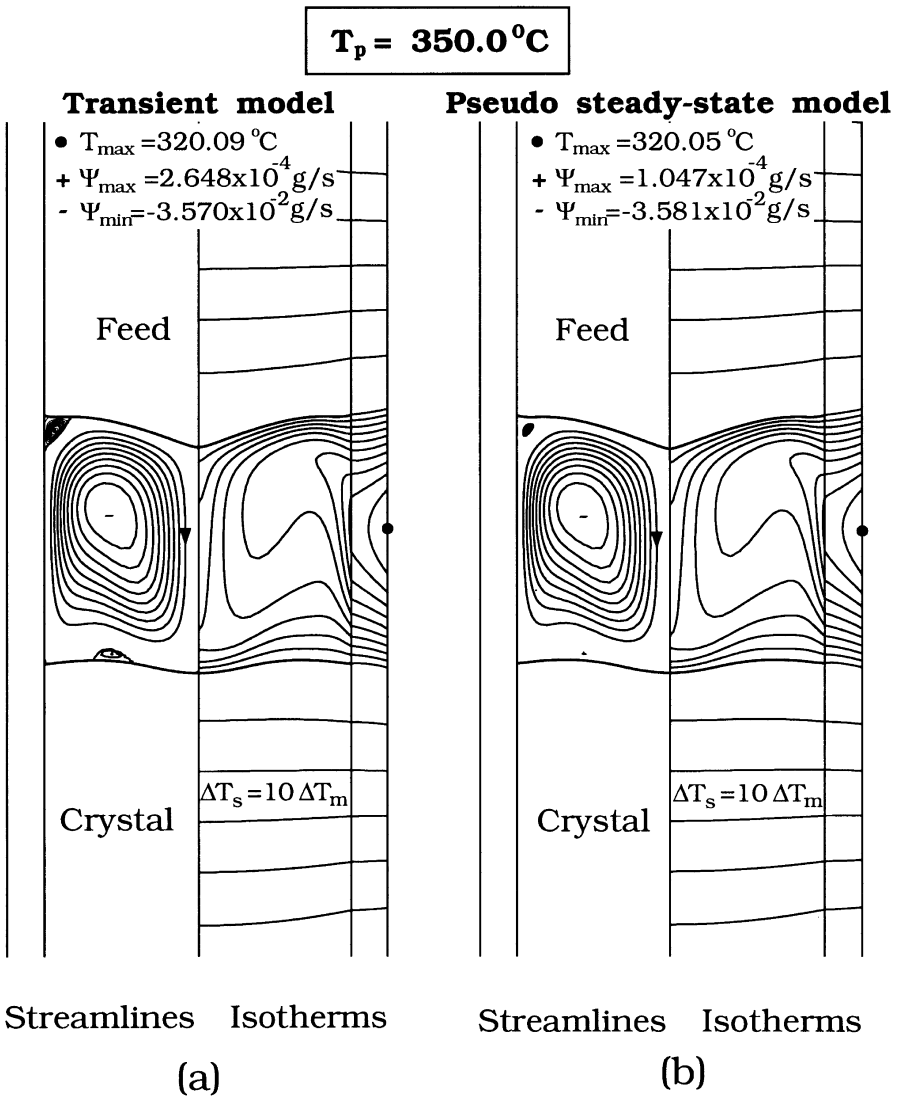


Fig. 11. Comparison of the steady-state solution from the fully transient model with that from the pseudo steady-state model [11].

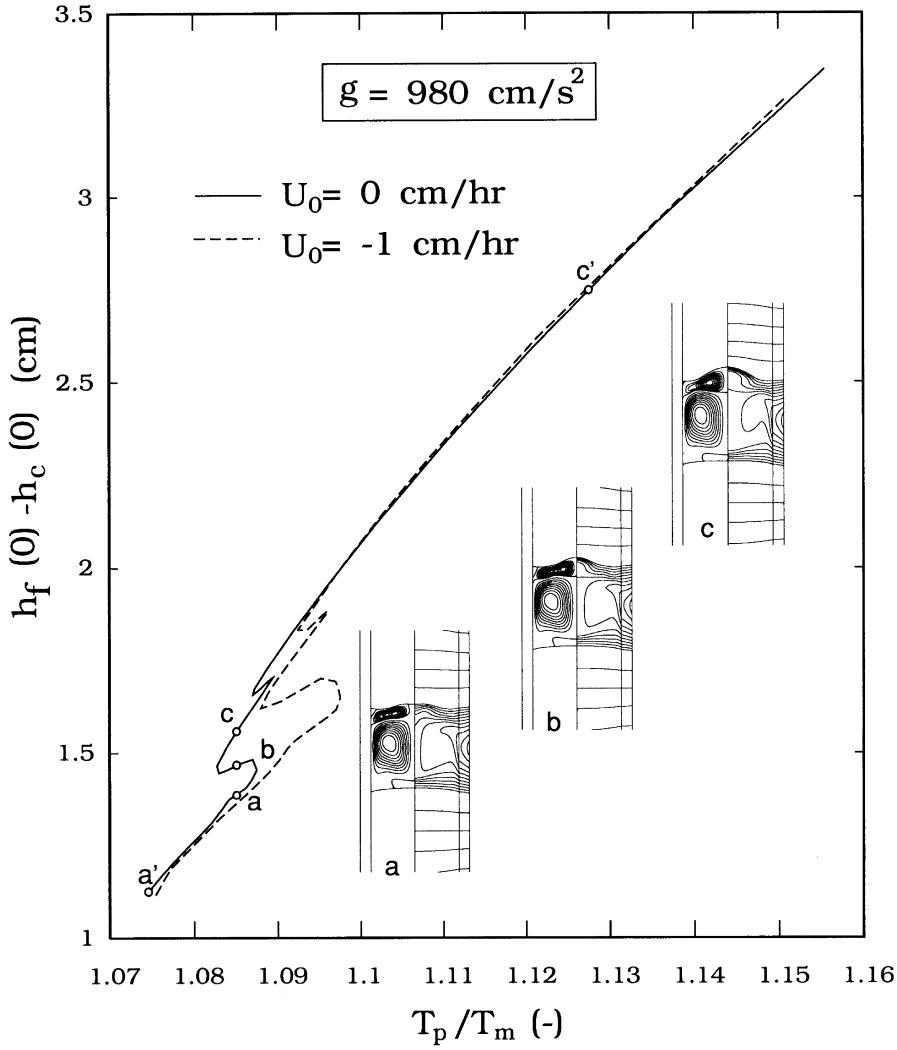


Fig. 12. Effect of peak heater temperature on the zone length under normal gravity; point a′ is the same as the point c in Fig. 9.

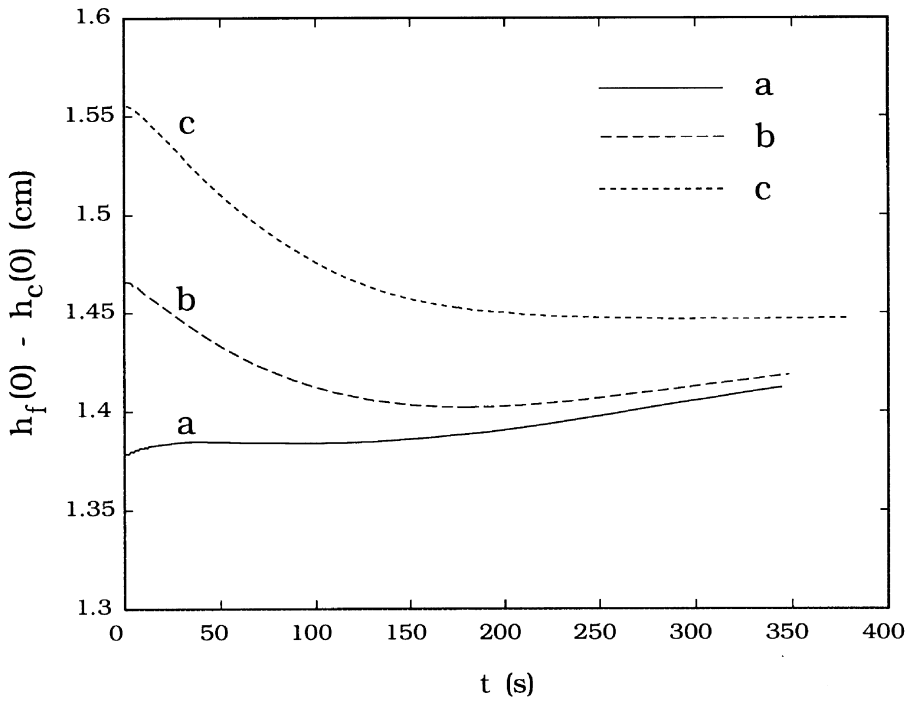


Fig. 13. Dynamic response of the zone length to the pulse change on the heater temperature. The initial conditions are from the basic states of Fig. 12.

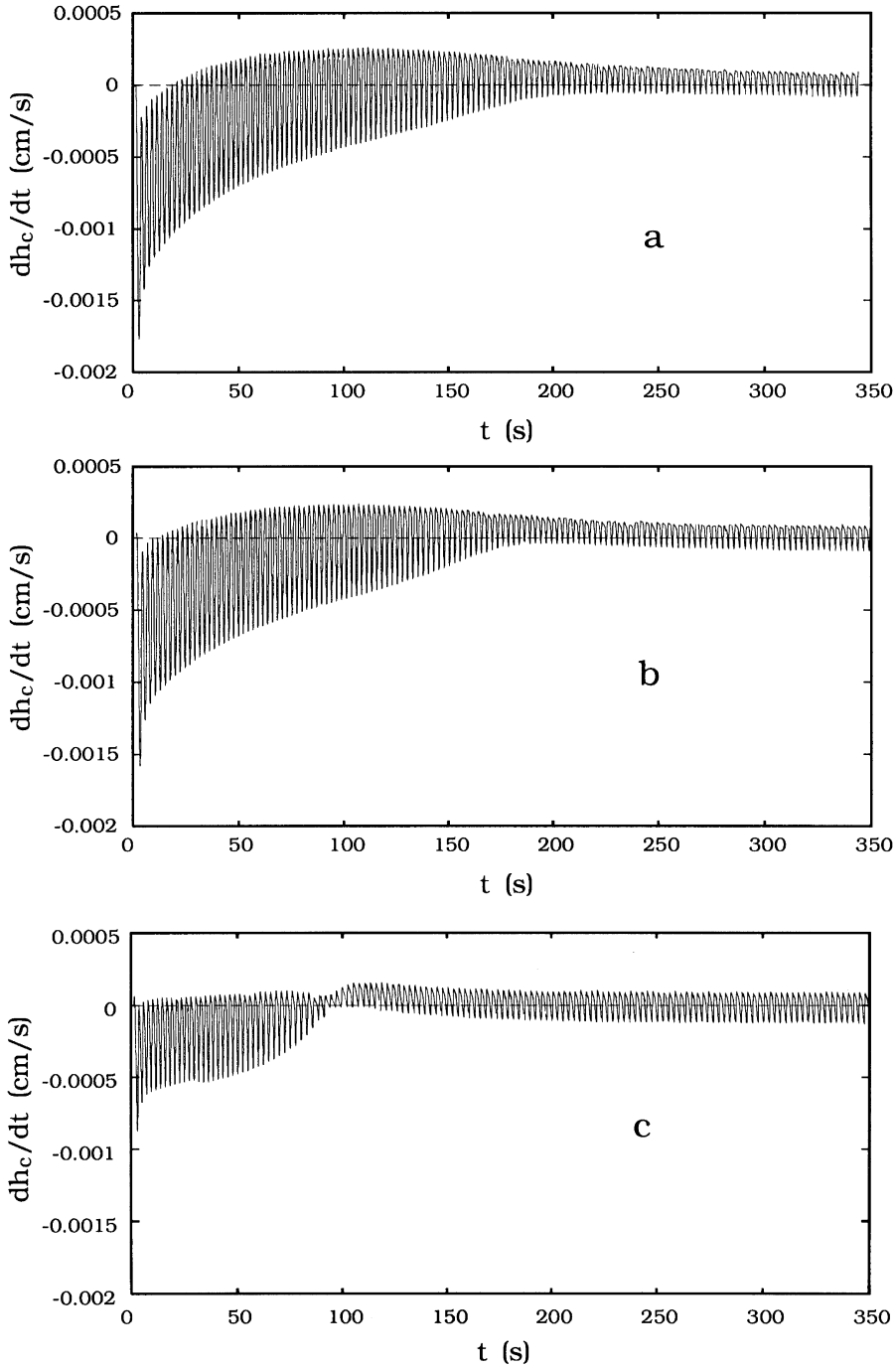


Fig. 14. Dynamic response of the growth rate to the pulse change on the heater temperature. The initial conditions are from the basic states of Fig. 12.

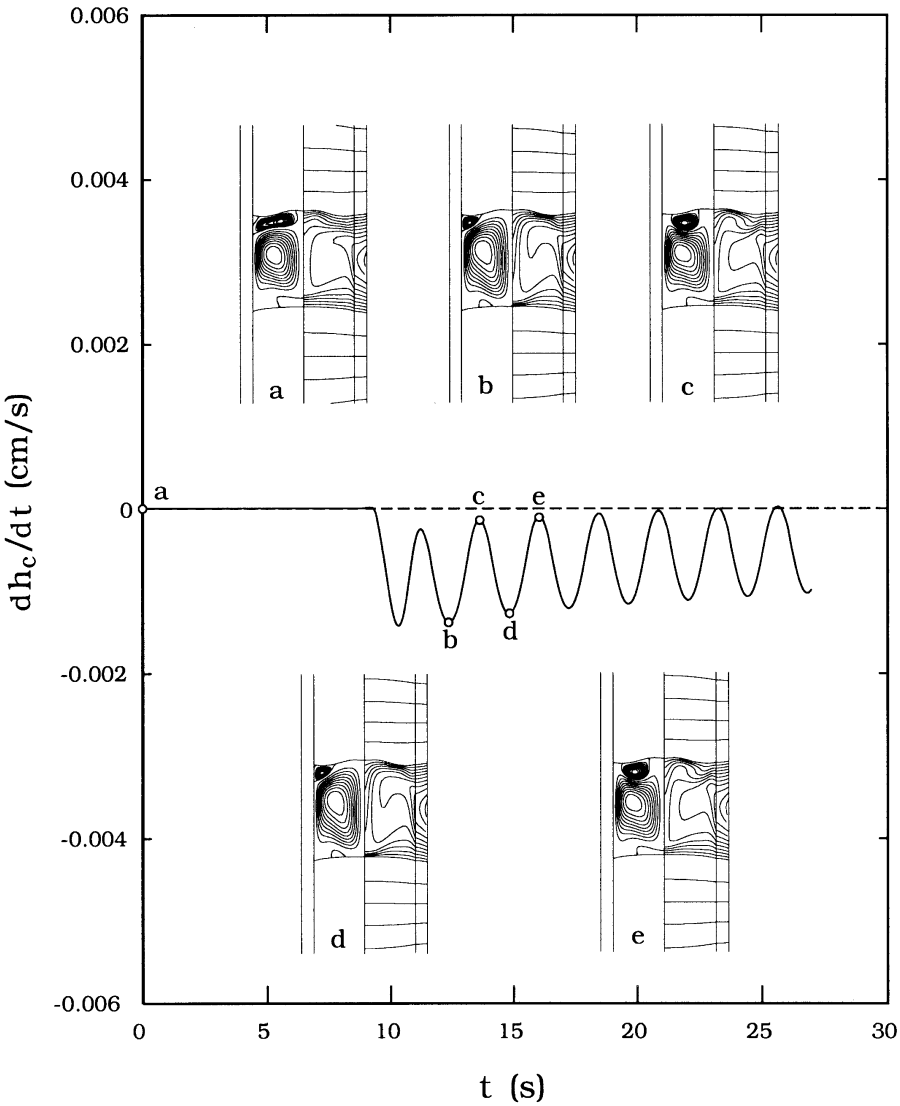


Fig. 15. Dynamic response of the growth rate and the associated flow patterns and isotherms of the basic state a of Fig. 12 to the step change on the heater moving speed $U_{heater}$.

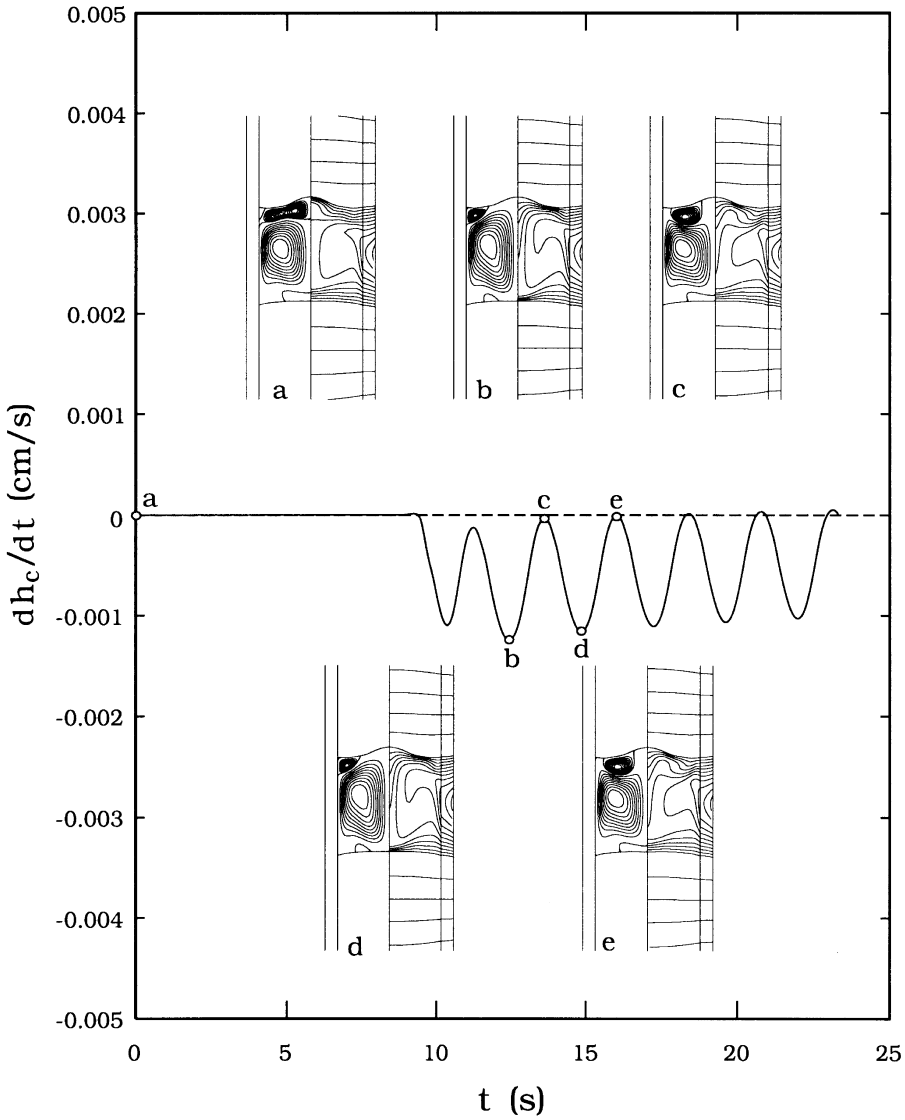


Fig. 16. Dynamic response of the growth rate and the associated flow patterns and isotherms of the basic state b of Fig. 12 to the step change on the heater moving speed $U_{heater}$.

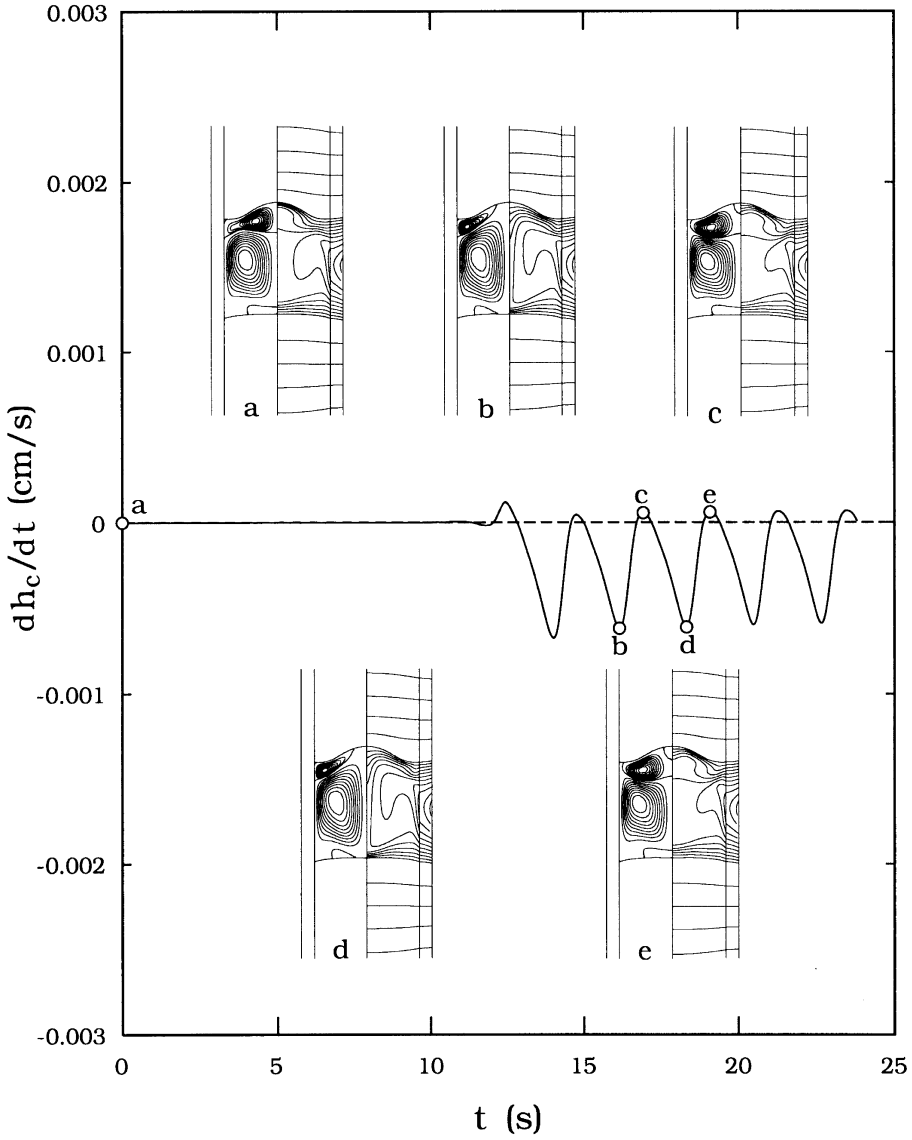


Fig. 17. Dynamic response of the growth rate and the associated flow patterns and isotherms of the basic state c of Fig. 12 to the step change on the heater moving speed $U_{heater}$.

## References

[1] Pfann WG. Zone Melting. 2nd ed. New York: John Wiley and Sons, 1966. p. 50.
[2] Johnson ES. Liquid encapsulated floating zone melting of GaAs. J Crystal Growth 1975;30:249–56.
[3] Henry RL, Nordquist PER, Gorman RJ, Qadri SB. Growth of (100) GaAs by vertical zone melting. J Crystal Growth 1995;109:228–33.
[4] Colombo L, Chang RR, Chang CJ, Baird BA. Growth of Hg-based alloys by the traveling heater method. Vacuum Sci Technol 1988;A6:2795–9.
[5] Yip, VFS, Chang CE, Wilcox WR. Heat and mass transfer in the traveling heater method of crystal growth. J Crystal Growth 1975;29:69–74.
[6] Boeck T, Rudolph P. The influence of thermal diffusion on the traveling heater method in a diffusion controlled growth system. J Crystal Growth 1986;79:105–9.
[7] Bell RO. An analysis of the temperature distribution during crystal growth by THM. J Electrochem Soc 1974;121:1366–71.
[8] Wald FV, Bell RO. Natural and forced convection during solution growth of CdTe by the traveling heater method (THM). J Crystal Growth 1975;30:29–36.
[9] Chang CJ, Baird B, Liao PK, Chang R, Colombo L. Finite element thermal analysis on the crystal growth of HgCdTe

by the traveling heater method. J Crystal Growth 1989;98:595–609.
[10] Apanovich YV, Ljumkis ED. The numerical simulation of heat and mass transfer during growth of a binary system by the traveling heater method. J Crystal Growth 1991;110:839–54.
[11] Lan CW, Yang DT. Numerical Investigation on heat transfer, fluid flow, and interfaces in vertical zone melting crystal growth. Numerical Heat Transfer Part A 1996;29:131–146.
[12] Lan CW, Yang DT. Computer simulation of crystal growth by traveling solvent method (TSM): pseudo steady-state calculations. Modeling and Simulation in Materials Sci and Eng 1995;3:71–92.
[13] Lan CW, Yang DT, Ting CC, Chen FC. A transparent multizone furnace for crystal growth and flow visualization. J Crystal Growth 1994;142:373–8.
[14] Gosman AD, Pan WM, Runchall AK, Spalding DB, Wolfshtein M. Heat and mass transfer in recirculating flows. London: Academic Press, 1969. p. 18.
[15] Lan CW. Newton's method for solving heat transfer, fluid flow and interface shapes in a floating molten zone. Intern J Numer Methods Fluids 1994;19:41–65.
[16] Petzold LR. An adaptive moving grid method for one-dimensional systems of partial differential equations and its numerical solution. Proceedings of the Workshop on Adaptive Methods for Partial Differential Equations, Rensselaer Polytechnic Institute, October, 1988.
[17] Petzold LR. A description of DASSL: a differential/algebraic system solver. In: Stepleman RS et al, editors. Scientific computing. Amsterdam: North-Holland, 1983. pp. 65–8.
[18] Brown PN, Saad Y. Hybrid Krylov methods for nonlinear systems of equations. SIAM J Sci Stat Comput 1990;11:450–81.
[19] Meijerink JA, van der Vorst HA. An iterative solution method for linear equations systems of which the coefficient matrix is a symmetric M-Matrix. Math Comp 1977;31:148–62.
[20] Coleman TF, Garbow BS, More JJ. Software for estimating sparse Jacobian matrices. ACM Trans Math Soft 1984;10:329–47.
[21] Derby JJ, Brandon S, Salinger AG, Xiao Q. Large-scale numerical analysis of materials processing systems: high-temperature crystal growth and molten glass flows. Comp Methods Appl Mech 1991;112:69–89.
[22] Muller G, Neumann G, Matz H. A two-Rayleigh-number model of buoyancy-driven convection in vertical melt growth configurations. J Crystal Growth 1987;84:36–49.
[23] Keller HB. Numerical solution of bifurcation and nonlinear eigenvalue problems. In: Rabinowitz PH, editor. Applications of bifurcation theory. New York: Academic Press, 1977.
[24] Yamaguchi Y, Chang CJ, Brown RA. Multiple buoyancy-driven flows in a vertical cylinder heated from below. Philos Trans Roy Soc London Ser A 1984;312:519–52.
[25] Muller G, Neumann G. Suppression of doping striations in zone melting of InSb crystals by enhanced convection on a centrifuge. J Crystal Growth 1982;59:548–56.
[26] Muller G, Neumann G. Tenfold growth rates in the traveling heater method of GaSb crystal growth by forced convection on a centrifuge. J Crystal Growth 1983;63:58–66.